

Magnetic field effects on particle beams and their implications for dose calculation in MR-guided particle therapy

Hermann Fuchs^{a)}

Department of Radiation Oncology, Medical University of Vienna/AKH, Vienna, Austria

Christian Doppler Laboratory for Medical Radiation Research for Radiation Oncology, Medical University of Vienna, Vienna, Austria

Philipp Moser

Department of Radiation Oncology, Medical University of Vienna/AKH, Vienna, Austria

Christian Doppler Laboratory for Medical Radiation Research for Radiation Oncology, Medical University of Vienna, Vienna, Austria

Institute of Applied Physics, Vienna University of Technology, Vienna, Austria

Martin Gröschl

Institute of Applied Physics, Vienna University of Technology, Vienna, Austria

Dietmar Georg

Department of Radiation Oncology, Medical University of Vienna/AKH, Vienna, Austria

Christian Doppler Laboratory for Medical Radiation Research for Radiation Oncology, Medical University of Vienna, Vienna, Austria

Comprehensive Cancer Center, Medical University of Vienna/AKH, Vienna, Austria

(Received 19 August 2016; revised 5 January 2017; accepted for publication 6 January 2017; published 16 March 2017)

Purpose: To investigate and model effects of magnetic fields on proton and carbon ion beams for dose calculation.

Methods: In a first step, Monte Carlo simulations using Gate 7.1/Geant4.10.0.p03 were performed for proton and carbon ion beams in magnetic fields ranging from 0 to 3 T. Initial particle energies ranged from 60 to 250 MeV (protons) and 120 to 400 MeV/u (carbon ions), respectively. The resulting dose distributions were analyzed focusing on beam deflection, dose deformation, as well as the impact of material heterogeneities. In a second step, a numerical algorithm was developed to calculate the lateral beam position. Using the Runge–Kutta method, an iterative solution of the relativistic Lorentz equation, corrected for the changing particle energy during penetration, was performed. For comparison, a γ -index analysis was utilized, using a criteria of 2%/2 mm of the local maximum.

Results: A tilt in the dose distribution within the Bragg peak area was observed, leading to non-negligible dose distribution changes. The magnitude was found to depend on the magnetic field strength as well as on the initial beam energy. Comparison of the 3 T dose distribution with non-B field (nominal) dose distributions, resulted in a γ_{mean} (mean value of the γ distribution) of 0.6, with 14.4% of the values above 1 and $\gamma_1\%$ (1% of all points have an equal or higher γ value) of 1.8. The presented numerical algorithm calculated the lateral beam offset with maximum errors of less than 2% with calculation times of less than 5 μ s. The impact of tissue interfaces on the proton dose distributions was found to be less than 2% for a dose voxel size of $1 \times 1 \times 1 \text{ mm}^3$.

Conclusion: Non-negligible dose deformations at the Bragg peak area were identified for high initial energies and strong magnetic fields. A fast numerical algorithm based on the solution of the energy-corrected relativistic Lorentz equation was able to describe the beam path, taking into account the particle energy, magnetic field, and material. © 2017 American Association of Physicists in Medicine [https://doi.org/10.1002/mp.12105]

Key words: carbon ion, characterization, ion beam therapy, magnetic field, MR, proton

1. INTRODUCTION

The role and importance of magnetic resonance imaging (MRI) in radiation oncology is rapidly increasing. Compared to existing and widespread X-ray-based solutions for image-guided radiotherapy, it offers superior soft tissue contrast without additional dose to the patient. Repeated imaging using MR allows high precision treatments and facilitates adaptive radiotherapy approaches and tumor motion

tracking^{1,2}. For precision photon beam therapy, the combination of an MR and treatment delivery system is already ongoing. For example, a commercial system combining a 0.35 T MR and three cobalt sources is already in clinical operation^{3,4} and clinical prototypes of an integrated hybrid MR-linac system are close to commercialization.^{5–7} The combination of magnetic fields with radiation therapy poses several challenges in patient positioning, treatment work-flow, treatment planning, and dose delivery. Consequently, MR-guided

radiotherapy has become a key research topic that also stimulates particle beam therapy.^{8,9}

It has already been shown that proton beam deflections due to magnetic fields cannot be neglected in dose calculation.⁷ A first approach to account for magnetic field deflections in treatment planning was published recently.^{12,17} However, these attempts were based on field free plan optimization and magnetic field corrections were applied only in a separate postoptimization step¹⁰ or by using a multistep full MC approach for identifying beam entrance angles and dose optimization, respectively.¹¹ In order to increase dose calculation precision and to avoid lengthy manual plan tuning, magnetic field effects need to be integrated directly into the dose calculation and optimization. Wolf et al.¹² showed that an analytical approach is able to describe the proton beam trajectory in a homogeneous magnetic field.

The use of analytical models has become standard in modern treatment planning system for dose calculation in particle therapy; some are also being developed to investigate novel treatment options.^{13,14} In this manuscript, we present a generic numerical algorithm that accurately models the behavior of a particle beam in an arbitrary magnetic field, which was subsequently applied to proton and carbon ion beams. Furthermore, extensive parameterization of additional beam effects in the presence of a magnetic field was performed, such as the influence on secondary fragments. The analytic algorithm can be directly used in a treatment planning system for dose calculation during optimization of scanned particle beam therapy, i.e., inverse treatment planning.

2. MATERIALS AND METHODS

2.A. Monte Carlo

Reference as well as benchmarking data for the subsequent numerical algorithm development were generated by Monte Carlo (MC) simulations. A custom-modified development version of GATE 7.1 alongside Geant4 10.0 patch 03 was used for all simulations. GATE is a MC platform based

on the Geant4 framework,¹⁵ developed by the OpenGATE collaboration.¹⁶ Data analysis was performed using the ROOT framework in version 5.34/24.¹⁷ All simulations were performed utilizing the QGSP_BERT_EMV physics list with 10^7 primary particles and a voxel size of 0.5 mm in lateral and longitudinal direction, respectively. Simulations investigating material interfaces were performed with a resolution of 0.5 mm in the area of interest, allowing to investigate also small effects by low-energetic particles such as electrons. The statistical uncertainty was below 3% for areas receiving more than 10% of the total dose.

The simulations were performed on an in-house computer grid as well as on the Vienna Scientific Cluster 2, a High-Performance Computing (HPC) cluster designed to cover the computing demands of scientific projects.

2.B. Irradiation geometries

A particle beam with an initially Gaussian shape of $\sigma = 3$ mm was assumed, with beam diversion set to zero, which impinged on a rectangular water phantom of $350 \times 350 \times 420$ mm³ alongside the z-axis. The phantom was placed in a homogeneous magnetic field along the y-axis, perpendicular to the initial beam direction. A sketch of the used setup is depicted in Fig. 1. Simulations were performed with mono-energetic proton and carbon ion beams. Initial energies of 60, 150, and 250 MeV for protons and 120, 250, and 400 MeV/u for carbon ions were chosen with respect to the energy ranges available at the Austrian particle therapy center, MedAustron.^{18–20}

Magnetic fields of 0, 0.35, 1, and 3 T were investigated, covering the range of clinical usage from low-field open MR systems up to high-field diagnostic devices.

Particle beams experience repeated scattering events during penetration of matter. The resulting effects within magnetic fields were studied using two-dimensional xz-projected dose distributions. An energy spectrum analysis alongside the lateral x-axis was performed both close to the beam entrance ($z = 10$ mm) and at the Bragg peak area. For comparison, a

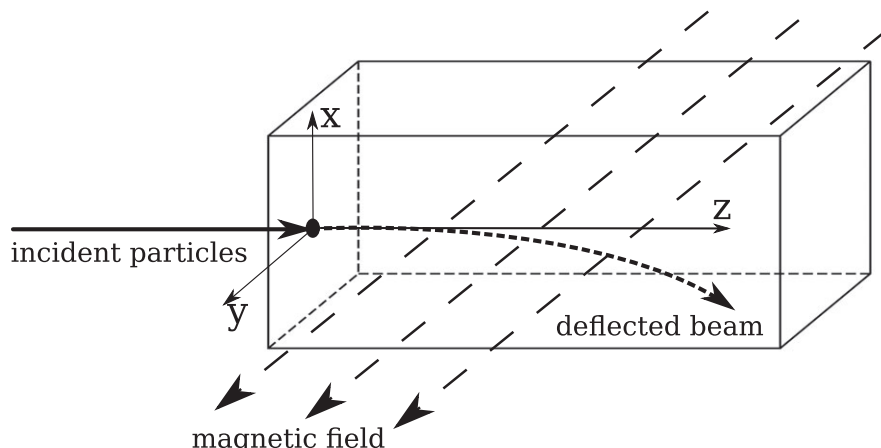


Fig. 1. Schematic illustration of the employed geometrical setup. The continuous arrow marks the initial beam direction, while the dashed arrows indicate the magnetic field orientation. For reference, the direction of beam deflection is indicated by a dotted line.

γ -index evaluation using a criterion of 2%/2 mm of the local maximum was performed, comparing the Bragg peak area of a beam experiencing a 3 T magnetic field and without a magnetic field, respectively. To do so, the dose distributions were aligned such that the center of the Bragg peak area coincided. Afterwards, to account for changing beam directions due to beam deflection, the nominal dose distributions were rotated, so that the beam directions in the Bragg peak region coincided. In order to avoid artifacts due to noise, values close to zero, being more than a factor of 7 lower than the maximal dose, were excluded from the γ -index evaluation.

Magnetic fields can lead to noticeable dose deposition modifications at the boundaries between the two materials due to the electron return effect (ERE).^{7,21} Effects of a 30-mm air cavity slab, located 200 mm after the water phantom entrance were studied for 250 MeV protons exposed to a homogeneous 3 T magnetic field. The electron production cutoff was set to 1 μm to investigate the effects of even very low-energetic, i.e., short-ranged electrons. Percentage depth dose (PDD) curves and two-dimensional dose maps were used to study the dose deposition difference at the material transitions.

2.C. Secondary particles

Magnetic fields may not only affect the primary charged particles but also any charged secondary particles, such as electrons or fragments, which can potentially change the dose distribution. The simulation phantom was longitudinally divided into three equally spaced subvolumes ($350 \times 350 \times 140 \text{ mm}^3$) distributed alongside the beam path, in order to take into account the progressive energy loss of the primary beam. Secondary electrons, helium, and oxygen fragments created during irradiation in the respective subvolumes were recorded.

The produced secondary particles as well as their energy spectrum were analyzed and converted into ranges according to the energy-range databases ESTAR, ASTAR, and PSTAR.^{22,23} The obtained ranges were evaluated to determine non-negligible track lengths which could potentially impact the dose distribution within a magnetic field.

2.D. Numerical beam deflection calculation

For ion beam dose calculation in magnetic fields, beam deflection curves yielding the lateral beam deviation are of great interest. For clinical use, full MC simulations and subsequent dose map analyses are time-consuming. Thus, a fast numerical algorithm was developed. The approximation of beam deflection curves was performed by solving the relativistic equations of motion taking into account the Lorentz force

$$\frac{d}{dt}(\Gamma m_0 \vec{v}) = q(\vec{v} \times \vec{B}) \quad (1)$$

where $\Gamma = (1 - \frac{|\vec{v}|^2}{c^2})^{-\frac{1}{2}}$ is the Lorentz factor and m_0 is the rest mass of a particle with charge q and velocity \vec{v} . Particle

energy correction was performed after each propagation step, using the Bethe–Bloch formula $\frac{dE}{ds}$:

$$\vec{v}_{\text{new}} = \vec{v}_{\text{old}} - \frac{d\vec{r}}{dx + dy + dz} \times (|\vec{v}_{\text{old}}| - |\vec{v}(\Gamma')|) \quad (2)$$

with

$$\Gamma' = \Gamma_{\text{old}} - \frac{1}{m_0} \int_0^d \frac{dE}{ds} ds \quad (3)$$

where d is the distance traveled in one step.

The Bethe–Bloch formula is sensitive with respect to the choice of correction terms below 1 MeV. Protons with an energy of 1 MeV have a residual range in water of less than 0.03 mm. For such small residual ranges, the contribution to the lateral deviation even of high angular deviations can be neglected. Therefore, a cutoff was introduced at $E_{\text{cut}} = 1 \text{ MeV}$.

The arising differential equations were iteratively solved by the Runge–Kutta (RK) algorithm, a numerical, discrete forth-order method.²⁴ The iterative calculation allows to account for changing magnetic fields as well as heterogeneous tissues as present in a patient.

3. RESULTS

3.A. Beam shape effects

The beam shape for protons was found to differ from the shape expected in the presence of magnetic fields. The resulting dose differences were located in two areas of the Bragg peak region, showing a tilt of the dose distribution as illustrated in Fig. 2.

A γ -index evaluation of the dose distribution of a 250 MeV proton beam within a 3 T field compared with the corresponding nominal dose distribution (see Fig. 2(b)), resulted in a γ_{mean} (mean value of the γ distribution) of 0.6, with 14.4% of the values above 1 and $\gamma_{\text{1\%}}$ (1% of all points have an equal or higher γ value) of 1.8. For lower field strengths, the differences observed in the dose distributions were smaller and less pronounced, as shown in Table I.

In the presence of magnetic fields, at beam entrance, the initially mono-energetic beam showed a constant and laterally symmetric energy distribution throughout the central beam profile (see Fig. 3(a)). The central part of the 2D phase space containing most of the protons was symmetric and circular, see Fig. 3(a). Right before the Bragg peak — at a penetration depth of 350 mm — the energy/proton distribution symmetry was lost and an energy rise alongside the beam profile was observed (see Fig. 3(b)). The depicted data were recorded perpendicular toward the incident particle energy. Protons on the outward beam side showed energies of up to 20 MeV higher compared to the inner side of the rotation plane. This resulted in laterally increasing proton ranges, i.e., in a deformed Bragg peak area shape. This effect was also reflected in the elliptically shaped and tilted phase space, see Fig. 3(b). Despite the lateral energy differences within the beam profile, the beam profile was still mostly Gaussian shaped. At a distance of two sigma from the beam,

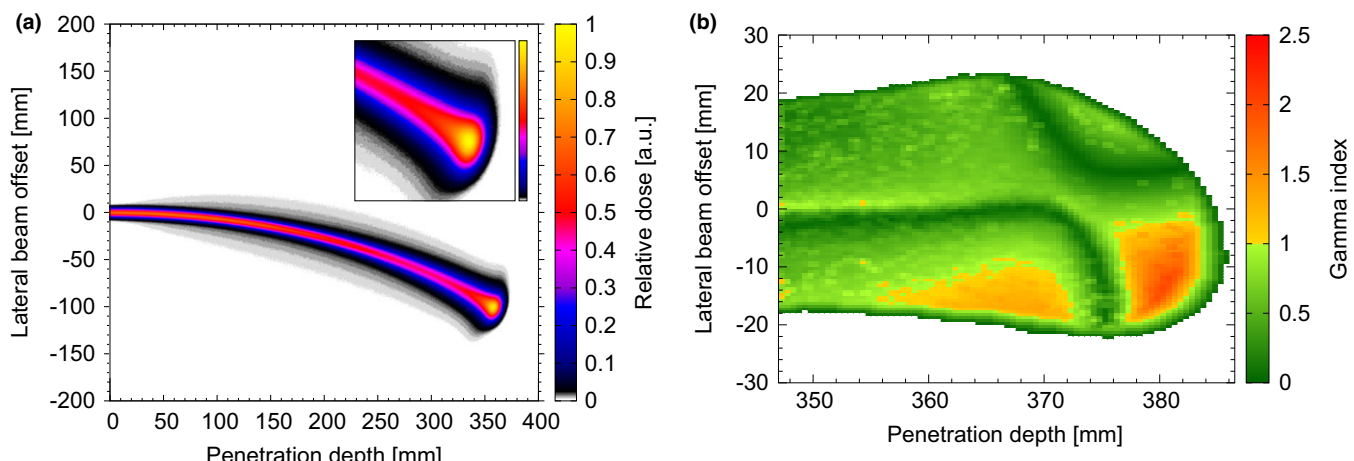


Fig. 2. (a) Dose deposition for a 250 MeV proton beam in water encountering a 3 T magnetic field. The smaller picture displays the zoomed Bragg peak region. (b) γ -index distribution using a criteria of 2%/2 mm compared to a Bragg peak region without magnetic field which was rotated and offset to match the beam angle and position at the Bragg peak area. [Colour figure can be viewed at wileyonlinelibrary.com]

TABLE I. γ -index comparison of the dose distribution of a beam experiencing a magnetic field and a reference beam rotated to coincide with the Bragg peak.

Mag. field	γ_{mean}	$\gamma_{1\%}$	$\gamma > 1$	γ_{max}
0.35 T	0.3	0.9	0.6	1.8
1 T	0.3	1.0	1.0	2.0
3 T	0.6	1.8	14.4	2.1

differences of 3.5% were found in lateral symmetry with deviations too small to be visible by eye.

Although the beam path was bent in the presence of a magnetic field, a deformation of the Bragg peak area itself was not observed for carbon ions.

3.B. Numerical beam path calculation

The lateral and longitudinal offsets of the Bragg peak defined at the dose maximum, of the incident particle beams are summarized in Table II for protons and in Table III for carbon ions, respectively.

Applying the numerical beam deflection algorithm including the particle energy loss correction presented above, resulted in a very good agreement with the Monte Carlo calculated reference curves (see Fig. 4). For protons, a mean error of 1.1% was determined, with a standard deviation of 0.6%. The respective values for carbon ions are 0.9% for the mean error with a standard deviation of 0.5%. The agreement was found to depend only slightly on the incident particle energy, with a maximum error of less than 2% for the highest initial energies and magnetic field strengths.

3.C. Secondary particle range

The energy distributions of secondary particles are shown in Fig. 5 for electrons, helium and oxygen ions. Ranges

below 0.1 mm were not simulated for efficiency reasons. The mean electron energy of 0.18 MeV corresponded to a range of 0.36 mm, while the maximum energies observed at 0.7 MeV corresponded to an electron range of 2.8 mm. In the Bragg peak region, the maximum electron energy dropped to 0.3 MeV corresponding to 0.84 mm.

For helium nuclei, the mean energy of about 1.25 MeV/u corresponded to a range of 0.04 mm, while the maximum energy observed of 10 MeV/u correlated to a track length of 1.24 mm. ^{16}O fragments showed to be low energetic with maximum energies of about 0.06 MeV/u, resulting a negligible range in the order of μm .

3.D. Material boundaries

The laterally integrated dose deposition for a 250 MeV proton beam with and without a 3 T field is depicted in Fig. 6. Directly before the air cavity, a dose increase at the left side of the water-air boundary was observed for the 3 T field. This peak corresponded to a dose increase of about 6% of the lateral integrated dose, taking into account all contributions of this slice. However, the corresponding dose difference in the center of the beam was found to be less than 2%. For a voxel size of $1 \times 1 \times 1 \text{ mm}^3$, similar values than reported earlier⁷ were found.

4. DISCUSSION

GATE/Geant4 allows the use of different physics lists for simulations. A physics list recommended by the Geant4 collaboration was used.^{25,26} While the validity of the use of GATE/Geant4 for proton beam therapy was already shown, so far no experimental data of a proton beam in a magnetic field are available. However, Geant4 is heavily used in high-energy physics and thoroughly tested in magnetic fields.²⁷ MR-guided proton therapy poses additional challenges compared to MR-guided photon-based therapy, as the primary

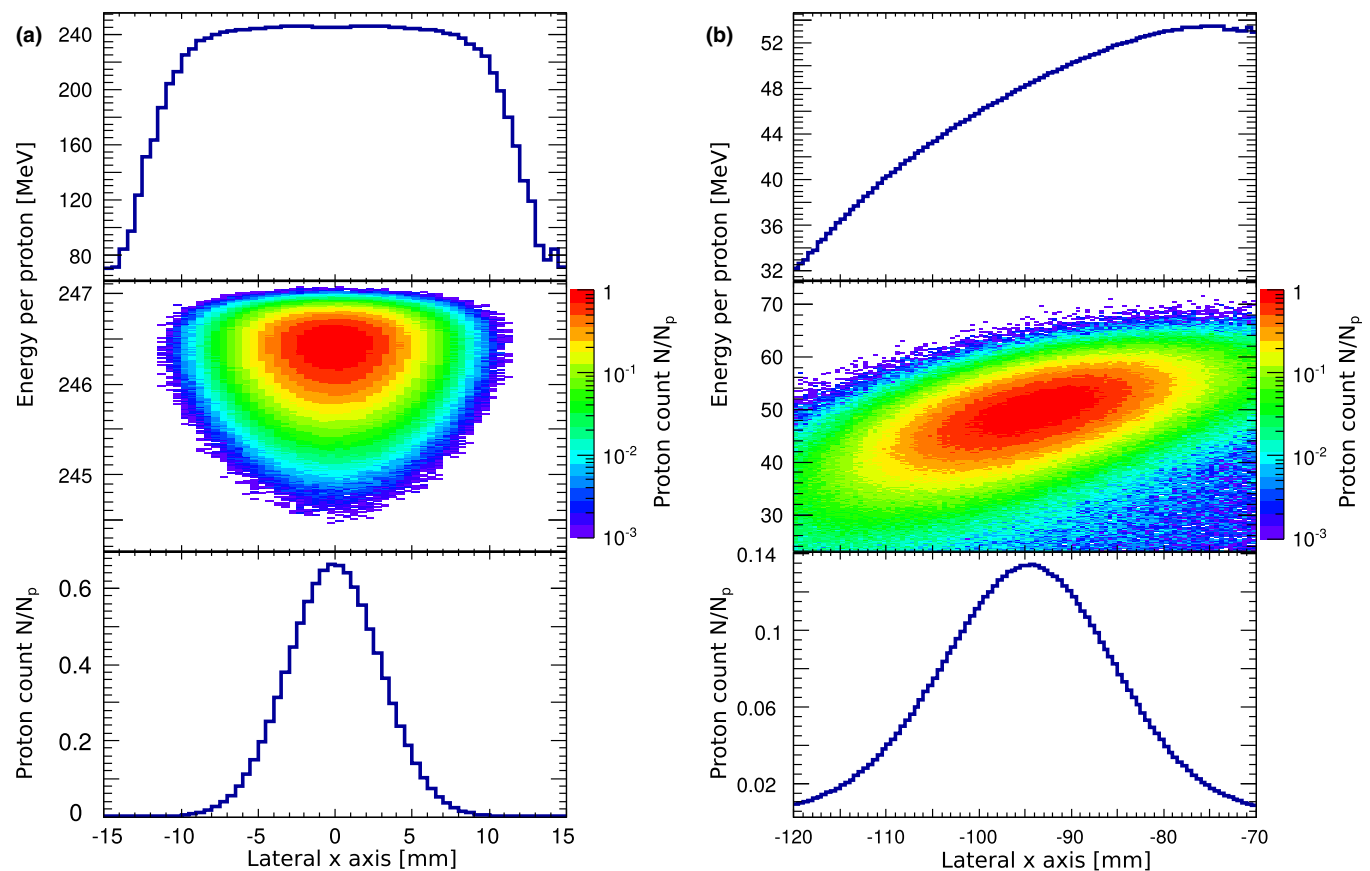


FIG. 3. Energy spectrum of a 250 MeV proton beam traversing a water phantom in a 3T magnetic field, (a) after the water entrance at 10-mm depth and (b) before the Bragg peak at 350-mm depth recorded perpendicular to the incident beam direction. Each graph depicting from top to bottom the energy per proton distribution, phase space, and particle count distribution. [Colour figure can be viewed at wileyonlinelibrary.com]

TABLE II. Simulated lateral and longitudinal Bragg peak locations for a proton beam in water of 60, 150, and 250 MeV initial energy for four magnetic field strengths.

Magnetic field	60 MeV [mm]	150 MeV [mm]	250 MeV [mm]
0 T	Lat.	0.0	0.0
	Long.	30.6	156.5
0.35 T	Lat.	0.2	2.5
	Long.	30.6	156.0
1 T	Lat.	0.5	7.3
	Long.	30.6	155.0
3 T	Lat.	1.4	22.8
	Long.	30.5	153.0

TABLE III. Simulated lateral and longitudinal Bragg peak locations for a carbon beam in water of 120, 250, and 400 MeV/u initial energy for four magnetic field strengths.

Magnetic field	120 MeV/u [mm]	250 MeV/u [mm]	400 MeV/u [mm]
0 T	Lat.	0.0	0.0
	Long.	34.8	124.5
0.35 T	Lat.	0.0	0.7
	Long.	34.8	124.4
1 T	Lat.	0.2	1.9
	Long.	34.8	124.3
3 T	Lat.	0.7	5.7
	Long.	34.8	124.1

treatment beam itself is directly influenced by the magnetic field. The origin of the observed dosimetric difference at the Bragg peak is multiple Coulomb scattering, leading to an energy variance resulting in the well-known range straggling. The presence of a magnetic field acted like an energy separator, guiding the lower energetic particles toward the inner side of the bending plane. The effect was immediately obvious for strong magnetic fields and high initial particle energies, but became less dominant for lower field strengths and particle energies. This is due to the higher particle range, where even a smaller angular direction change results in an overall larger

lateral deviation. For magnetic fields in the order of 0.35 T, which is a common field strength of clinically used open MR scanners, it might be even possible to neglect this effect for dose calculation.

Due to their increased mass, carbon ions were much less sensitive to range straggling. In addition, the lower charge to mass ratio resulted in a much lower sensitivity to magnetic fields, e.g., smaller overall bending radii and consequently less difference between particles. Therefore, a deformation of the Bragg peak area as for protons was not observed.

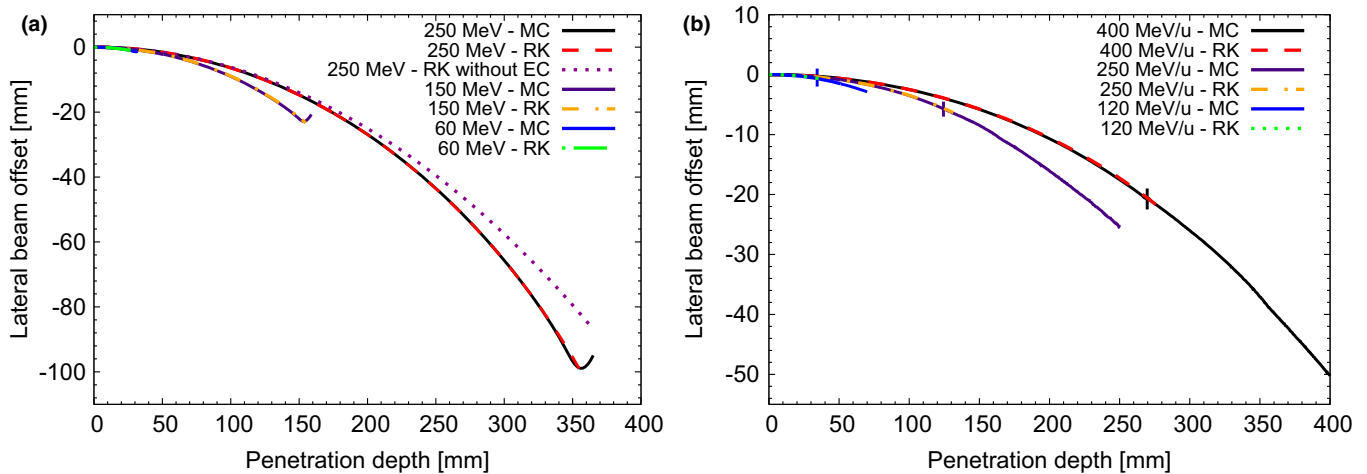


FIG. 4. Comparison of the Runge–Kutta calculation of the beam deflection for a (a) 60, 150, and 250 MeV proton beam and a (b) 120, 250, and 400 MeV/u carbon ion beam in water experiencing a magnetic field of 3 T. The solid lines represent the dose maximum at the given penetration depths, while the dashed curve depicts the numerical calculated values. The rise at the end of the proton reference data is due to a deformation of the Bragg peak area described above which was not modeled in the numerical approach. In (b), the Bragg peak depth is indicated by a small bar. [Colour figure can be viewed at wileyonlinelibrary.com]

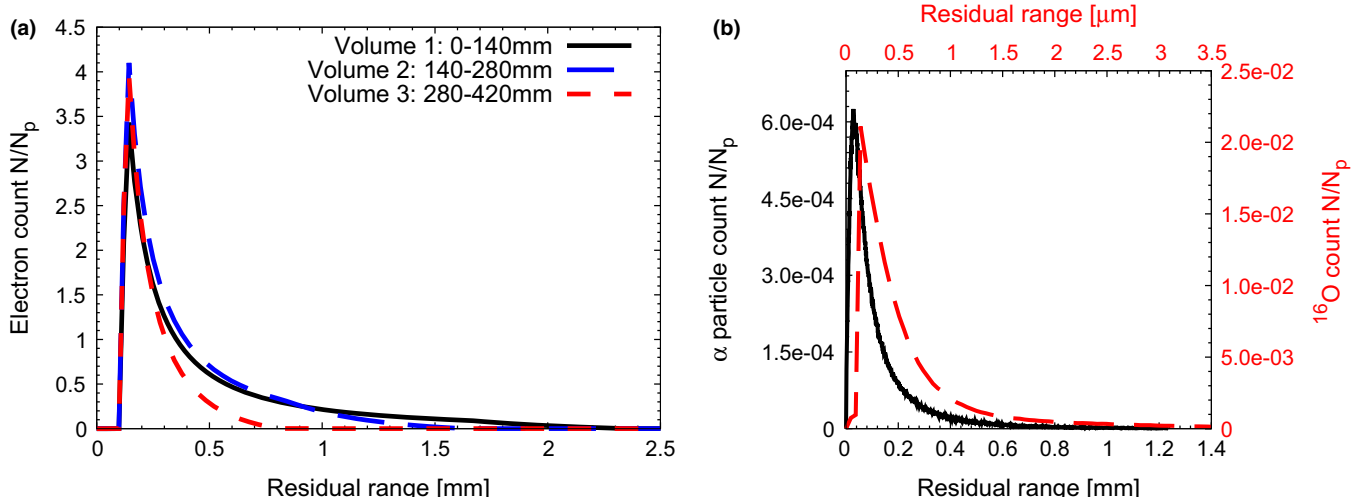


FIG. 5. Residual range distribution of (a) secondary electrons measured in the beam entrance, plateau, and Bragg peak region and (b) helium and oxygen ions of a 250 MeV proton beam in water. [Colour figure can be viewed at wileyonlinelibrary.com]

As can be seen in Fig. 4(a), the reference curve tilts upwards at the Bragg peak position. This was caused by the deformation of the Bragg peak area described above, resulting in a shift of the dose maximum, commonly used to determine the beam center. As this was a multiparticle effect, it was not modeled directly by our pencil beam (PB) algorithm, but could be corrected in a dose calculation algorithm, e.g., by calculating more trajectories with slightly different energies.

Although such magnetic field effects can be described using MC methods, MC-based dose calculation requires significant amount of time and resources, making it challenging to implement in clinical routine. Up to now, most treatment planning systems in particle beam therapy still use fluence-based semi-analytical algorithms for dose calculation. Especially for optimization purposes such PB algorithms will

continue to be employed due to their paramount calculation speed.

A previously published method¹² reported lateral deviations of the beam path of 3.7% for a 200 MeV proton beam, whereas our algorithm, for the same setup, could reduce the lateral deviation by half, to less than 1.8% for a comparable magnetic field strength. For comparison, a simple scaling by the applied magnetic field to convert lateral offsets between magnetic fields resulted in differences of up to 5% with respect to the reference curves. The good agreement confirms the suitability of the presented algorithm for deflection curve calculation.

In literature,⁷ no difference of the electron spectra resulting from proton beams was reported, which might be explained by the use of higher cuts, limited data points, as well as the generally lower energies investigated. As can be

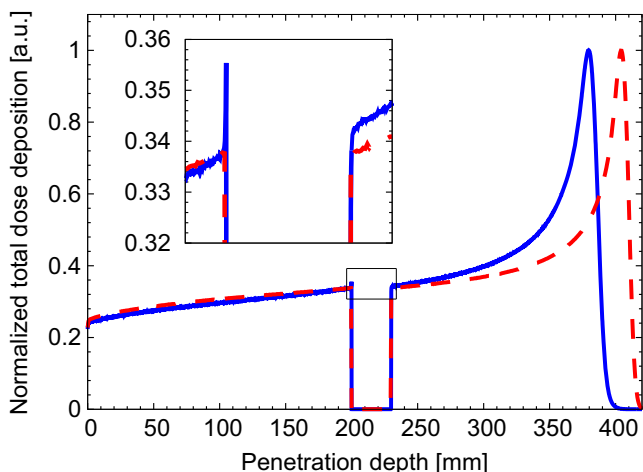


Fig. 6. Laterally integrated dose distribution for a 250 MeV proton beam in a water phantom with 30-mm air cavity, with and without a magnetic field. The solid line corresponds to an applied magnetic field of 3 T, the dashed continuous line corresponds to no applied magnetic field. Due to magnetic bending, the range of the particle beams does not coincide. [Colour figure can be viewed at wileyonlinelibrary.com.]

easily seen in Fig. 5(a), the secondary electron energy distribution shifted toward lower energies at progressing penetration depths. Energy and momentum conservation caused the produced secondary electrons to be less energetic, as primary protons progressively lost energy during penetration. Only electrons resulting from all charged secondary particles were found to have non-negligible ranges, potentially influencing the dose distribution shape at boundary regions. Secondary protons were not analyzed in detail, as they behave similar to the primary protons and no additional effects were found.

For carbon ions, more secondary fragments were created due to the fragmentation of the primary beam particles. However, all fragments heavier than protons were found to be negligible in terms of residual range (median range smaller than 0.05 mm). Electron distributions were found to be of similar energy and range as from proton beams. Secondary protons exhibited high particle ranges. However, only about 5% of the incident carbon ions created a proton and the smaller dose contribution of protons compared to carbon ions, limited the change in the overall dose contribution.

Further investigation confirmed that the dose increase at material borders was caused by the returning of high-energy electrons. However, a 10 MV photon beam showed almost 7 times higher dose differences compared to protons. It should be kept in mind that the presented case, employing the highest proton energy as well as the strongest magnetic field, pronounced the differences. For lower energies and magnetic fields, the effects should be even smaller. This effect will result in a lower skin dose when using charged particles as opposed to photons, as reported earlier.^{21,28} The absence of an higher entrance dose at the distal end of the cavity of the air cavity depicted in Fig. 6 can be explained by the residual electron range of less than 2 mm and the applied magnetic field, hindering electrons to reach the distal end of the cavity.

However, the impact of cavities needs to be studied in more detail to explore the effect on varying cavity size, position, and incident particle energy.

The magnetic field of a diagnostic MR scanner was recently modeled, which could be used as a template for future proton MR combinations.²⁹ It was demonstrated that only a small volume of the magnetic field inside such a hybrid system will be homogeneous. This is especially important as fringe fields might start to influence the treatment beam already quite far away from the patient. Therefore, non-homogeneous magnetic fields need to be taken into account by any dose calculation algorithm.

In addition, there may be reverse influences of magnetic fields on transport lines and nozzle elements, which are beyond the scope of this manuscript. The iterative calculation of the particle propagation presented here, allows to account for varying environment parameters at each step. The calculation speed of the presented algorithm should not be influenced by inhomogeneous magnetic fields or density heterogeneities, as Eq. (1) is evaluated on a per step basis. Consequently, the significant calculation time difference will be preserved. Therefore, the presented algorithm is well suited for taking into account the magnetic field effects in the presence of a clinical environment, either in final dose calculation of a treatment planning system, or for intermediate dose calculation during inverse treatment planning.

5. CONCLUSION

In the presence of a magnetic field, energy differences within the primary ion beam caused deformations of the Bragg peak area. For high initial energies and strong magnetic fields, these effects cannot be neglected. Range analysis of secondary charged particles showed that only electrons influence the dose distribution, especially at material borders. However, the impact was found to be below 2% at any given voxel, for the highest energies and magnetic fields evaluated. The presented fast numerical method is feasible for dose calculation of particle beam in the presence of magnetic fields, taking into account varying, heterogeneous magnetic fields and material heterogeneities.

ACKNOWLEDGMENTS

The computational results presented have been achieved in part using the Vienna Scientific Cluster (VSC). We thank MOCCAMED group for providing access to their cluster enabling MC simulations and evaluations in reasonable time. The financial support by the Federal Ministry of Science, Research and Economy and the National Foundation for Research, Technology and Development is gratefully acknowledged.

CONFLICT OF INTEREST

The authors have no conflict of interest to report.

^aAuthor to whom correspondence should be addressed. Electronic mail: hermann.fuchs@meduniwien.ac.at.

REFERENCES

1. Lagendijk JJ, Raaymakers BW, Raaijmakers AJ, et al. MRI/linac integration. *Radiother Oncol*. 2016;86:25–29.
2. Yun J, Wachowicz K, Mackenzie M, Rathee S, Robinson D, Fallone BG. First demonstration of intrafractional tumor-tracked irradiation using 2D phantom MR images on a prototype linac-MR. *Med Phys*. 2013;40:051718-1–051718-12.
3. Mutic S, Dempsey JF. The viewray system: magnetic resonance-guided and controlled radiotherapy. *Seminars in Radiation Oncology*. 2014;24:196–199.
4. Wooten HO, Green O, Yang M, et al. Quality of intensity modulated radiation therapy treatment plans using a 60Co magnetic resonance image guidance radiation therapy system. *Int J Radiat Oncol Biol Phys*. 2015;92:771–778.
5. Kolling S, Oborn B, Keall P. Impact of the MLC on the MRI field distortion of a prototype MRI-linac. *Med Phys*. 2013;40:121705–123569.
6. Raaymakers BW, Lagendijk JJW, Overweg J, et al. Integrating a 1.5 T MRI scanner with a 6 MV accelerator: proof of concept. *Phys Med Biol*. 2009;54:N229–N237.
7. Raaymakers BW, Raaijmakers AJE, Lagendijk JJW. Feasibility of MRI guided proton therapy: magnetic field dose effects. *Phys Med Biol*. 2008;53:5615–5622.
8. Kontaxis C, Bol GH, Lagendijk JJW, Raaymakers BW. Towards adaptive IMRT sequencing for the MR-linac. *Phys Med Biol*. 2015;60:2493.
9. Smit K, Sjöholm J, Kok JGM, Lagendijk JJW, Raaymakers BW. Relative dosimetry in a 1.5 T magnetic field: an MR-linac compatible prototype scanning water phantom. *Phys Med Biol*. 2014;59:4099.
10. Moteabbed M, Schuemann J, Paganetti H. Dosimetric feasibility of real-time MRI-guided proton therapy. *Med Phys*. 2014;41:111713.
11. Hartman J, Kontaxis C, Bol GH, et al. Dosimetric feasibility of intensity modulated proton therapy in a transverse magnetic field of 1.5 T. *Phys Med Biol*. 2015;60:5955–5969.
12. Wolf R, Bortfeld T. An analytical solution to proton Bragg peak deflection in a magnetic field. *Phys Med Biol*. 2012;57:N329–N337.
13. Fuchs H, Alber M, Schreiner T, Georg D. Implementation of spot scanning dose optimization and dose calculation for helium ions in Hyperion. *Med Phys*. 2015;42:5157–5166.
14. Fuchs H, Ströbele J, Schreiner T, Hirtl A, Georg D. A pencil beam algorithm for helium ion beam therapy. *Med Phys*. 2012;39:6726.
15. Agostinelli S, Allison J, Amako K, et al. GEANT4 – A simulation toolkit. *Nucl Instrum Methods Phys Res A*. 2003;506:250–303.
16. Jan S, Benoit D, Becheva E, et al. GATE V6: a major enhancement of the GATE simulation platform enabling modelling of CT and radiotherapy. *Phys Med Biol*. 2011;56:881–901.
17. Antcheva I, Ballintijn M, Bellenot B, et al. ROOT - A C++ framework for petabyte data storage, statistical analysis and visualization. *Comput Phys Commun*. 2009;180:2499–2512.
18. Benedikt M, Wrulich A. Medaustron-project overview and status. *Eur Phys J Plus*. 2011;126:1–11.
19. Schreiner T, Seemann R. MedAustron – Ion-beam therapy and research center; 2015.
20. Stock M, Georg P, Mayer R, Böhnen TT, Vatnitsky S. Development of clinical programs for carbon ion beam therapy at MedAustron. *Int J Part Ther*. 2015;2:474–477.
21. Raaijmakers AJE, Raaymakers BW, Lagendijk JJW. Magnetic-field-induced dose effects in MR-guided radiotherapy systems: dependence on the magnetic field strength. *Phys Med Biol*. 2008;53:909.
22. Andersen HH, Ziegler JF. *Hydrogen Stopping Powers and Ranges in All Elements. Stopping and ranges of Ions in Matter*. Vol. 3. Elmsford, NY: Pergamon Press; 1977.
23. Berger MJ. *ESTAR, PSTAR, and ASTAR: computer programs for calculating stopping- power and range tables for electrons, protons, and helium ions*. Technical report; 1992.
24. Press WH, Teukolsky SA, Vetterling WT, Flannery BP. *Numerical Recipes: The Art of Scientific Computing*, 3rd edn. Cambridge: University Press, 2007.
25. Apostolakis J, Folger G, Grichine V, et al. GEANT4 physics lists for HEP. *IEEE Nucl Sci Symp Conf Rec*. 2008: 833–836.
26. Geant4 collaboration. *Physics lists – use cases – reference physics lists*; 2014.
27. Geant4 collaboration. *Physics validation and verification*; 2016.
28. Oborn BM, Metcalfe PE, Butson MJ, Rosenfeld AB. Monte Carlo characterization of skin doses in 6 MV transverse field MRI-linac systems: effect of field size, surface orientation, magnetic field strength, and exit bolus. *Med Phys*. 2010;37:5208–5217.
29. Oborn BM, Dowdell S, Metcalfe PE, Crozier S, Mohan R, Keall PJ. Proton beam deflection in MRI fields: implications for MRI-guided proton therapy. *Med Phys*. 2015;42:2113–2124.